Nanoscale

PAPER

View Article Online
View Journal | View Issue

Cite this: *Nanoscale*, 2020, **12**, 9255

Achieving ferromagnetic insulating properties in $La_{0.9}Ba_{0.1}MnO_3$ thin films through nanoengineering†

Chao Yun, [a] Eun-Mi Choi, ‡[a] Weiwei Li,[a] Xing Sun, [b] Tuhin Maity, [a] Rui Wu, [a] Jie Jian, [b] Sichuang Xue,[b] Seungho Cho, §[a] Haiyan Wang [b] and Judith L. MacManus-Driscoll *[a]

Strongly correlated manganites have a wide range of fascinating magnetic and electronic properties, one example being the coexistence of ferromagnetic and insulating properties in lightly-doped bulk. However, it is difficult to translate bulk properties to films. Here, this problem is overcome by thin film nanoengineering of the test case system, $La_{0.9}Ba_{0.1}MnO_3$ (LBMO). This was achieved by using vertically aligned nanocomposite (VAN) thin films of LBMO + CeO_2 in which CeO_2 nanocolumns form embedded in a LBMO matrix. The CeO_2 columns produce uniform tensile straining of the LBMO. Also light Ce doping of intrinsic cation vacancies in the LBMO occurs. Together, these factors strongly reduced the double exchange coupling and metallicity. Hence, while standard plain reference films showed an insulator-to-metal transition at >200 K, originating from defects and complex structural relaxation, the VAN LBMO films exhibited ferromagnetic insulating properties (while maintaining a T_c of 188 K). This is the first time that a combined strain + doping method is used in a VAN system to realise exemplary properties which cannot be realised in plain films. This work represents an important step in engineering high performance spintronic and multiferroic thin film devices.

Received 28th September 2019,
Accepted 18th December 2019

DOI: 10.1039/c9nr08373a

rsc.li/nanoscale

Introduction

Ferromagnetic insulating (FMI) behaviour is required for spin filters and tunneling barriers in tunneling junctions as well other spintronic and multiferroic devices.[1,2] However, at practical operating temperatures the coexistence of ferromagnetism and insulating conductivity is very rare in known materials systems.[1,3] Examples of ferromagnetic insulators are $SeCuO_3$ (ferromagnetic Curie temperature, T_c ~25 K),[4] and EuO (T_c ~77 K),[5] but their relatively low T_cs hinder their application. Double perovskites (such as La_2CoMnO_6, T_c ~220 K), ferrites (such as $NiFe_2O_4$, T_c >300 K) and garnets (such as $Bi_3Fe_5O_{12}$, T_c >300 K) are good candidates with high T_cs,[6–8] but their complex structures, difficult growth conditions and moderate conductivity in thin film form makes them problematic. On the other hand, lightly doped manganites, $La_{1-x}A_xMnO_3$ (A = Ba, Ca and Sr) $0.05 < x < 0.2$, are promising materials because in bulk form they show ferromagnetic insulating (FMI) behaviour up to 200 K.[9] Also, they have a perovskite structure which is structurally compatible with widely available perovskite substrates of $SrTiO_3$-buffered Si, and other perovskite oxides with wide ranging functionalities for multifunctional devices.[10] However, bulk FMI properties are modified or vanished and cannot be translated to thin films,[11–13] and an anomalous metallic behaviour is observed with an insulator-to-metal (I–M) transition at a wide range of temperatures depending on the growth and heat treatment process. Indeed, the lack of ability to translate bulk properties to thin films is well-known in the broad range of manganite compositions,[14,15] and indeed in many other functional perovskites (including ferroelectrics and superconductors).[16,17]

A key reason for the thin film anomalies is the strong coupling between the charge, orbital and spin degrees of freedom,[18] making the properties highly tunable by chemical and physical pressure.[19–21] Hence, in films, strain and

[a]*Department of Materials Science and Metallurgy, University of Cambridge, Cambridge, CB3 0FS, UK. E-mail: jld35@cam.ac.uk*
[b]*Materials Engineering, Purdue University, West Lafayette, IN, 47907, USA*

†Electronic supplementary information (ESI) available: XPS valence band spectra for PF and NC, plan view EDS line profile for the La and Ce elements, Influence of Ce doping on the transport property, defect equations, structural information for the two thick films. Detailed structural analysis of the 100 nm PF using TEM (PDF). See DOI: 10.1039/c9nr08373a

‡Current address: Center for Integrated Nanostructure Physics, Institute of Basic Science, Sungkyunkwan University, Suwon 16419, Korea.
§Current address: School of Materials Science and Engineering, Ulsan National Institute of Science and Technology (UNIST), Ulsan 44919, Republic of Korea.

non-stoichiometry effects lead to strongly modified properties.[11,13,14,22–25] In fact, progress has been made in metallic (heavier doped) manganites to reduce the so-called "dead layer" thickness (present in ultrathin films), which is related to structural or non-stoichiometry effects,[26,27] but the inability to achieve insulating performance in lightly doped manganites still remains.

Here, we focus on the FMI candidate material of lightly doped $La_{1-x}Ba_xMnO_3$ ($0 < x < 0.2$), which lies in a narrow composition region where the physical properties are very sensitive to structural and compositional perturbations. For example, it has been reported that a 0.65% in-plane tensile strain enhances the T_c of $La_{0.9}Ba_{0.1}MnO_3$ by almost 100 K.[11] A similar case has been reported in lightly doped $La_{1-x}Sr_xMnO_3$.[14] Compared to lighted doped $La_{1-x}Sr_xMnO_3$ and $La_{1-x}Ca_xMnO_3$, lightly doped $La_{1-x}Ba_xMnO_3$ has a higher T_c,[9,12,28,29] *i.e.* T_c is ~185 K for x = 0.1, whereas it is <150 K for the same x value in $La_{1-x}Sr_xMnO_3$ and $La_{1-x}Ca_xMnO_3$. In lightly doped $La_{1-x}Ba_xMnO_3$, as mentioned above, even in relatively thick films (>100 nm) where epitaxial strain should be relaxed, metallicity exists.[11,12]

Recently, vertically aligned nanocomposites (VAN) have provided a new route to tune the physical properties of heteroepitaxial oxides. We aim to use the VAN concept[30,31] to achieve FMI property in LBMO thin films. The special properties of VAN films include:

1. A stiff nanocolumn embedded within a softer matrix can effectively tune both the out-of-plane (op) and in-plane (ip) strain states of the matrix phase.

2. While the matrix phase is initially clamped by the substrate ip, after a certain thickness the columns dominate the strain state of the matrix phase[32] both along the ip and op directions.[15,33] The columns act as "anchors" to maintain a stable and uniform strain state of the matrix, without inhomogeneity or relaxation, and without thickness limitation.[34]

3. Overall, the resulting 3D strain control is totally different to what is achievable in a plain film (PF).[15,35]

4. The vertical strain state can be easily controlled by changing growth conditions, phase ratio and film thickness, and the nanocolumn phase enables a uniform strain to be maintained even when the film is very thick.[32,36]

5. Vertical interfacial effects in VAN films are different to substrate/film effects in plain films. In VAN films, at the VAN vertical interface there is no evidence of the well-known "dead layer" effect that is observed in the substrate/film interface of very thin manganite films which reduces T_c. This is because the growth rate of VAN vertical interfaces is much slower than horizontal plain film/substrate interfaces. This likely enables misfit dislocations to form readily instead of other deleterious T_c-reducing defects.[37–39]

In PFs, on the other hand, strain is controlled only by the substrate, *i.e.* by the ip strain from epitaxial constraints, and the op strain is modified as a consequence of elastic effects. The strain is not uniform with film thickness and it relaxes gradually in a variety of ways as the film thickens. Since the formation energy of point defects is lower than misfit dislocations, and the octahedra in perovskite oxides have a high freedom of tilt/rotation, relaxation can occur by other phases forming, lattice modulation or by cation/oxygen vacancy generation.[39–42]

In this work, we show that when 50 at% CeO_2 is added to $La_{0.9}Ba_{0.1}MnO_3$ (LBMO), a self-assembled VAN nanocomposite (NC) film forms comprised of a LBMO matrix and with CeO_2 nanocolumns heteroepitaxially embedded in the matrix. The presence of the CeO_2 nanocolumns enabled the LBMO to be strained uniformly under tension. Also, light Ce doping on the La vacancy sites in the LBMO occured and reduced unwanted Mn^{4+} in the film. The strain and doping effects together reduce the double exchange (DE) coupling and enable the LBMO to retain the FMI properties. This was not the case for reference PFs which showed metallicity. The FMI properties achieved in this work have given a higher T_c (188 K) than that of the $Sm_{0.34}Sr_{0.66}MnO_3$ (140 K) achieved in our earlier work.[15] Furthermore, the LBMO system is chemically and structurally simpler than the $Sm_xSr_{1-x}MnO_3$ system.

CeO_2 was chosen as the strain controlling phase for LBMO as CeO_2 is stiffer than LBMO (the Young's modulus E_{CeO_2} = 220–240 GPa,[43,44] while the reported E for manganite is ~120–140 GPa (ref. 36, 45 and 46)), and thus in the VAN films CeO_2 is predicted to control the strain state of LBMO as reported in other similar systems.[32] The addition of CeO_2 was also deemed to be beneficial from a doping point of view: Ce substitution is known to substitute on the A (La) site in La manganites,[47] this being promoted by the known cation deficiency of the La site.[48]

Results and discussion

A series of LBMO PF and LBMO–CeO_2 NC films were made, and the thickness varied from 12 to >100 nm. Above ~50 nm, the film properties did not show further marked changes in functional performance but instead long time deposition may cause thermal annealing or strain relaxations. Hence, we mainly focus on the change in film properties up to ~50 nm.

Fig. 1a shows resistance *vs.* temperature (R–T) curves for two LBMO PFs. An I–M transition is present in the PF, and when the thickness is increased from 21 to 42 nm, the I–M transition temperature, T_M, remains almost constant at around 220–223 K (with a slight increase of 3 K), as shown by the arrow. This is consistent with the general trend in manganite thin films that relaxation occurs above a certain thickness, which leads to an almost constant T_M (T_c).[26] The existence of metallicity in the thicker PF indicates that, apart from the strain, there is another cause of the metallicity in the PF, which is likely non-stoichiometry.

The I–M transition (and the corresponding paramagnetic–ferromagnetic transition discussed later) occurs as a result of the DE coupling between Mn^{3+} and Mn^{4+} mediated by O.[49] The DE coupling in doped manganites is influenced by both doping and strain.[10] Charge-orbital ordering (COO), which is characteristic of lightly doped manganites,[50] occurs at a much lower temperature T_{COO} (here defined at the temperature where a minimum point is shown in the R–T curve at low

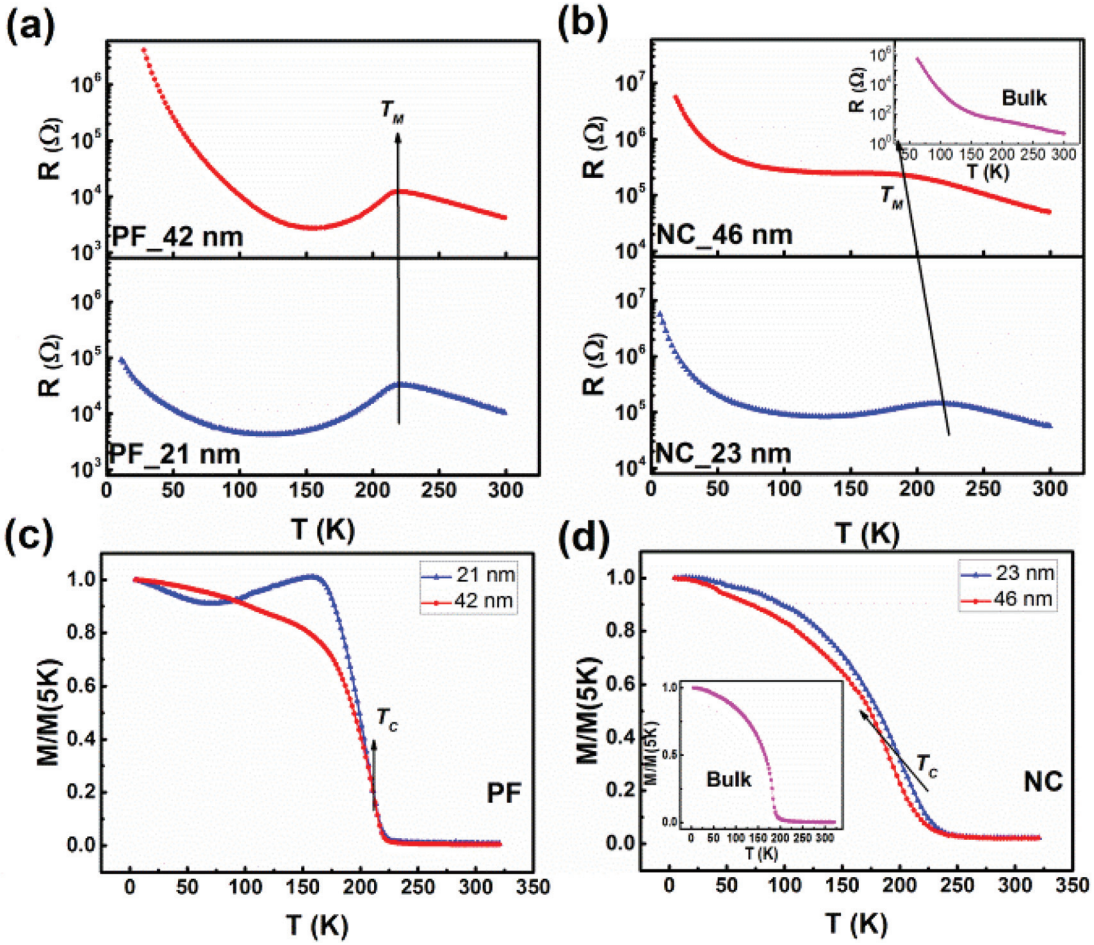

Fig. 1 Thickness dependence of the resistance *vs.* temperature (R–T) curves of (a) LBMO plain films (PFs) and (b) LBMO–CeO_2 nanocomposite (NC) films. The R–T curve for the LBMO bulk is also shown as a comparison. Thickness dependence of the field cooling M–T curves of (c) the LBMO PFs and (d) the LBMO–CeO_2 NC films. M–T curve for the LBMO bulk target is also shown for comparison. The applied field was 200 Oe.

temperatures). This brings about the observed resistance upturn in the PFs in Fig. 1a. The increase in T_{COO} with the increase in thickness: from 120 K (21 nm) to 155 K (42 nm) can be correlated to the change in the Jahn–Teller distortion caused by the change in the strain state.[50]

The resistance in Fig. 1 is not converted to resistivity due to the different nature of conductive paths (and different cross section areas for current flow) between the PF and NC. The R–T plot for two NC films and the $La_{0.9}Ba_{0.1}MnO_3$ bulk target (inset) are shown in Fig. 1b. The LBMO bulk is insulating, as expected. A thickness dependence is found in the NC films: a lower thickness (≤23 nm) favours a more metallic transport property while a larger thickness NC film (≥46 nm) gives insulating behaviour without any metallicity. The insulating and metallic behaviours are defined based on the slope of dR/dT, *i.e.* a negative slope indicates an insulating behaviour and a positive slope a metallic behavior. Since it is hard to determine the I–M transition temperature for the 46 nm NC, the T_M is estimated by extrapolating the inflection point in the R–T curve (the trend is shown by the arrow).

XPS valence band spectra near the Fermi level for the 42 nm PF and 46 nm NC films were also measured (see Fig. S1 in ESI S1†) to determine the valence-band maximum (VBM) values by linear extrapolation of the leading edge of the valence band region to the extended baseline of the spectra.[23] As illustrated by the dashed lines of Fig. S1,† the top of the valence band for the PF is higher than the NC, and there is higher density of states near Fermi level in the PF than in the NC, which indicates that the NC is more insulating than PF and is consistent with the transport measurements.

The temperature dependent magnetization (M–T) data for the PF and NC are shown in Fig. 1c and d. The applied magnetic field was 200 Oe and it was applied parallel to the substrate plane. The T_c, determined at the temperature where the dM/dT reaches the maximum, changes in a similar way as T_M: the T_c of PF remains almost constant at around 212 K (with a slight increase of 3 K) while the T_c of NC decreases from 201 K to 188 K when the thickness increases from 23 to 46 nm. The M–T curve for the $La_{0.9}Ba_{0.1}MnO_3$ bulk target is also included in the inset of Fig. 1d for comparison and a T_c of 182 K is observed, as expected for bulk of this composition.[51]

The magnetization *vs.* magnetic field (M–H) curves for the 42 nm-thick PF, 46 nm-thick NC, and LBMO bulk (target) measured at 5 K are shown in Fig. S2 in ESI S2.† Clearly M–H loops are observed, indicating that both PF and NC show ferromagnetism. The saturation magnetization of the NC is 2.75μ_B/Mn, which is somewhat lower than that of the bulk (3.65μ_B/Mn) and PF (3.52μ_B/Mn). This is likely due to the Ce doping or vertical strain discussed later.

Fig. 2a and b show TEM cross-sectional and plan view images for a 46 nm thick LBMO–CeO_2 nanocomposite. A clear

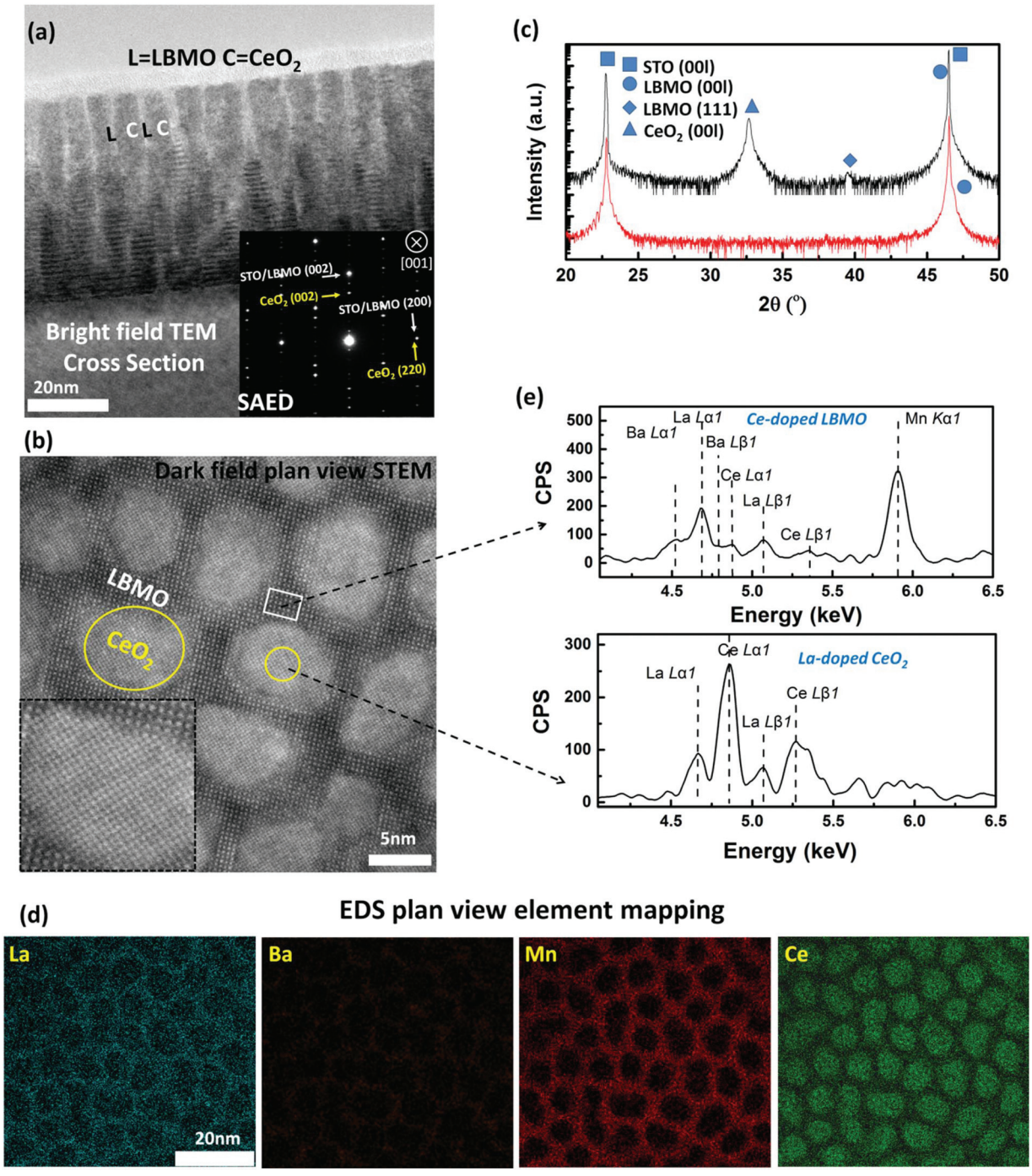

Fig. 2 (a) Bright-field TEM cross-section image of a 46 nm thick LBMO–CeO_2 nanocomposite. Inset: Selected area electron diffraction (SAED) index. (b) High resolution high angle annular dark-field plan view STEM image. The inset shows an enlarged planar STEM image of a CeO_2 pillar. (c) XRD ω–2θ scans for a 46 nm-thick LBMO–CeO_2 nanocomposite and a 42 nm-thick LBMO plain film. (d) Energy dispersive X-ray spectroscopy (EDS) plan view element mapping. (e) EDS element spectrum showing a small amount of Ce exists in the LBMO area (up) and La exists in the CeO_2 area (bottom).

phase separation and high-quality epitaxy are observed. The CeO_2 nanocolumns (average radius 6–8 nm) are densely distributed within a continuous LBMO matrix, and the average spacing between the CeO_2 nanocolumns is only ~3–6 nm. This structure is common when a manganite-binary oxide combination are coherently grown on a perovskite substrate.[52] The high crystalline quality of LBMO (and CeO_2) is clear from Fig. 2b (and the inset), as is the very large density interfaces with CeO_2.

From the selected area electron diffraction (SAED) pattern in the inset of Fig. 2a, the epitaxy relationship is determined to be: LBMO (001)//STO (001) and LBMO [100]//STO [100], CeO_2 (001)//STO (001) and CeO_2 [110]//STO [100]. As reported previously, the ip lattice constant of CeO_2 can be matched with STO after a 45° rotation.[53–55] It is noticeable that the diffraction spots of the (002) oriented STO are broadened compared with that of the STO single crystal, indicative of the close overlap of the LBMO and STO op diffraction spots because of the nearly perfect op lattice matching.

Fig. 2c shows the XRD 2θ–ω scans of a 46 nm LBMO–CeO_2 NC and a 42 nm LBMO PF grown under the same growth conditions. The thickness fringes of both LBMO and CeO_2 phases are shown in the NC indicative of a high quality epitaxy and smooth surface of both phases on the STO substrate. Apart from the LBMO (00l) phase, there is also a weak peak at 39.4° which is likely from the LBMO (111) phase.[56] Given the peak intensity of this phase is so low (<20 cps), the influence to the physical properties can be ignored. Plan view EDS element mapping is shown in Fig. 2d. These images further prove the clear phase separation.

Fig. 2e shows a local EDS spectrum. The La/Ce EDS line profile is shown in Fig. S3 in the ESI S3.† Ce doping of the LBMO phase is observed, and the level is estimated to be 5–10% Ce doping on the La site.

Also, La doping of the CeO_2 phase occurs on an estimated level of ~10–20%. We note that the op lattice parameter measured for CeO_2 in the 46 nm NC film (5.47 Å) is larger than the CeO_2 bulk value (5.41 Å), as determined from Fig. 2c. La^{3+} (117 pm) has a larger ionic radius than Ce^{4+} (101 pm), and it has been reported that the CeO_2 lattice parameter is expanded to ~5.44–5.48 Å when the La doping fraction in CeO_2 is 10–20%.[57,58] Hence, this agrees with the estimated La doping fraction in CeO_2 from EDS (Fig. 2e and Fig. S3†). We note that the CeO_2 phase is fully relaxed (data not shown here) in the ip direction due to the large lattice mismatch with STO (>1%), and therefore, the ip strain was not considered when inferring the Ce doping ratio from the op lattice constant. La-doped CeO_2 can be regarded as a dilute magnetic oxide but the magnetization is usually at least two orders of magnitude lower than in manganites,[59,60] and hence its contribution to the overall magnetic signal is insignificant.

It is now important to differentiate the effects of Ce doping and nanocolumn-induced strain on the electrical and magnetic properties. To learn about the Ce doping effect alone, two reference 100 nm-thick PFs were studied. The films were deposited using stoichiometric targets of $La_{0.85}Ce_{0.05}Ba_{0.1}MnO_3$ and $La_{0.8}Ce_{0.1}Ba_{0.1}MnO_3$. The growth condition was exactly the same as the nanocomposite and plain films in Fig. 1. A 100 nm thickness was chosen to eliminate additional epitaxial strain effects from the substrate.

Our result shows that CeO_2 was observed only in the XRD scan of the $La_{0.8}Ce_{0.1}Ba_{0.1}MnO_3$ film but not present in $La_{0.85}Ce_{0.05}Ba_{0.1}MnO_3$ (data not shown here). Hence, this indicates that the effective Ce doping level in our VAN films is between 5 and 10%. This is in agreement with the estimated Ce doping level from the EDS data, which is consistent with the limited solubility of Ce into the parent $LaMnO_3$ phase.[61,62] On the other hand, the reported solubility of La in CeO_2 is very high.[58] This explains our observed Ce doping level in LBMO being lower than the level of La in CeO_2.

The R–T curves of the 100 nm PFs (with Ce doping ratio varying from 0 to 5% and 10%) are shown in Fig. S4a,† and a 110 nm NC is shown in Fig. S4b.† The ~100 nm films show similar R–T behavior as the ~46 nm films: the metallicity and T_M (~224 K) is maintained in the PF while the NC remains insulating.

From Fig. S4a,† it is observed that compared to the LBMO film with no Ce doping, for Ce doping levels of 5% and 10%, T_M is reduced by 7 K and 18 K, respectively. T_c is also reduced by a similar amount (data not shown here). Also, the films become progressively more insulating with Ce doping, *i.e.* the resistance increases by an order of magnitude for the 10% Ce doping *cf.* the undoped PF.

The chemical/structural disorder caused by inhomogeneous Ce doping in manganites is well-known: it increases the overall resistance, but the disorder alone cannot well explain the decrease in T_M/T_c that we observe.[63,64] We consider Kröger–Vink[65] defect equations (ESI S4†) to explain. First, considering undoped manganite film, cation vacancies exist especially in the lightly doped region.[13] This explains the enhanced T_c (T_M) in the PF, *i.e.* La vacancies in the PF cause an increase in the Mn^{4+}/Mn^{3+} ratio and hence increase in the Mn^{3+}–O–Mn^{4+} DE coupling as compared to bulk. In the Ce-doped films, Ce^{3+} (or Ce^{4+}) substitution of the La vacancy sites reduces the amount of Mn^{4+}, thus suppressing the DE coupling, decreasing both T_c and T_M, and ultimately producing FMI LBMO films. Hence, the reason that Ce doping increases the resistance and decreases the T_M (T_c) of both the Ce-doped reference PFs in Fig. S4† and the NC films in Fig. 1c is well understood.

We now consider the vertical strain effect from the nanocolumns in the NC films. We observed that the form of R–T curves of the 100 nm Ce-doped reference PFs are very different from the 100 nm NC film (Fig. S4†). There is a clear I–M transition in the former (just as there is in other PFs) but not in the latter NC. We also note that ferromagnetic T_c of the 100 nm $La_{0.8}Ce_{0.1}Ba_{0.1}MnO_3$ (10% Ce doping) reference film is 195 K, which is 14 K higher than the 110 nm NC (T_c = 181 K). These results indicate that Ce doping of the PF reduces the DE coupling, but does not eliminate it and so the ferromagnetic insulating properties cannot be achieved by Ce-doping alone. Hence, vertical strain engineering in the NC films adds a further structural tuning effect.

To understand the vertical strain effect on the electrical and magnetic properties of the NC films further, we study how the strain of the NC films evolves with thickness. The 3D strain states of the NC and PF were analysed using asymmetric reciprocal space maps (RSM) around the STO (103) peaks, as well as symmetric 2θ–ω scans near the STO (003) peaks, as shown in Fig. 3a–d. Here two thicknesses ~20 nm and ~40 nm were analysed. The dashed lines in Fig. 3a–d show the trends of the lattice parameters with film thickness. The XRD data of a 100 nm PF and a 110 nm NC are also shown in Fig. S5 in ESI S6† to support the analysis.

It is clear from Fig. 3a and c that the PFs contain diffraction peaks from three phases: two tetragonal phases (A and A′) that are both ip strained by the STO, as observed by the same Q_x positions in the RSMs of Fig. 3a, although some ip relaxation is observed in phase A′ at 100 nm thickness (Fig. S5a†). The other phase is a twinning phase, labelled T. A schematic film structure showing the location of three phases in the PFs is shown in Fig. 3e. For reasons explained below, we predict that A lies at substrate surface and is fully strained by it, and A′ lies above the initial A layer region, while the T phase starts to appear from a certain thickness (as discussed later). Detailed

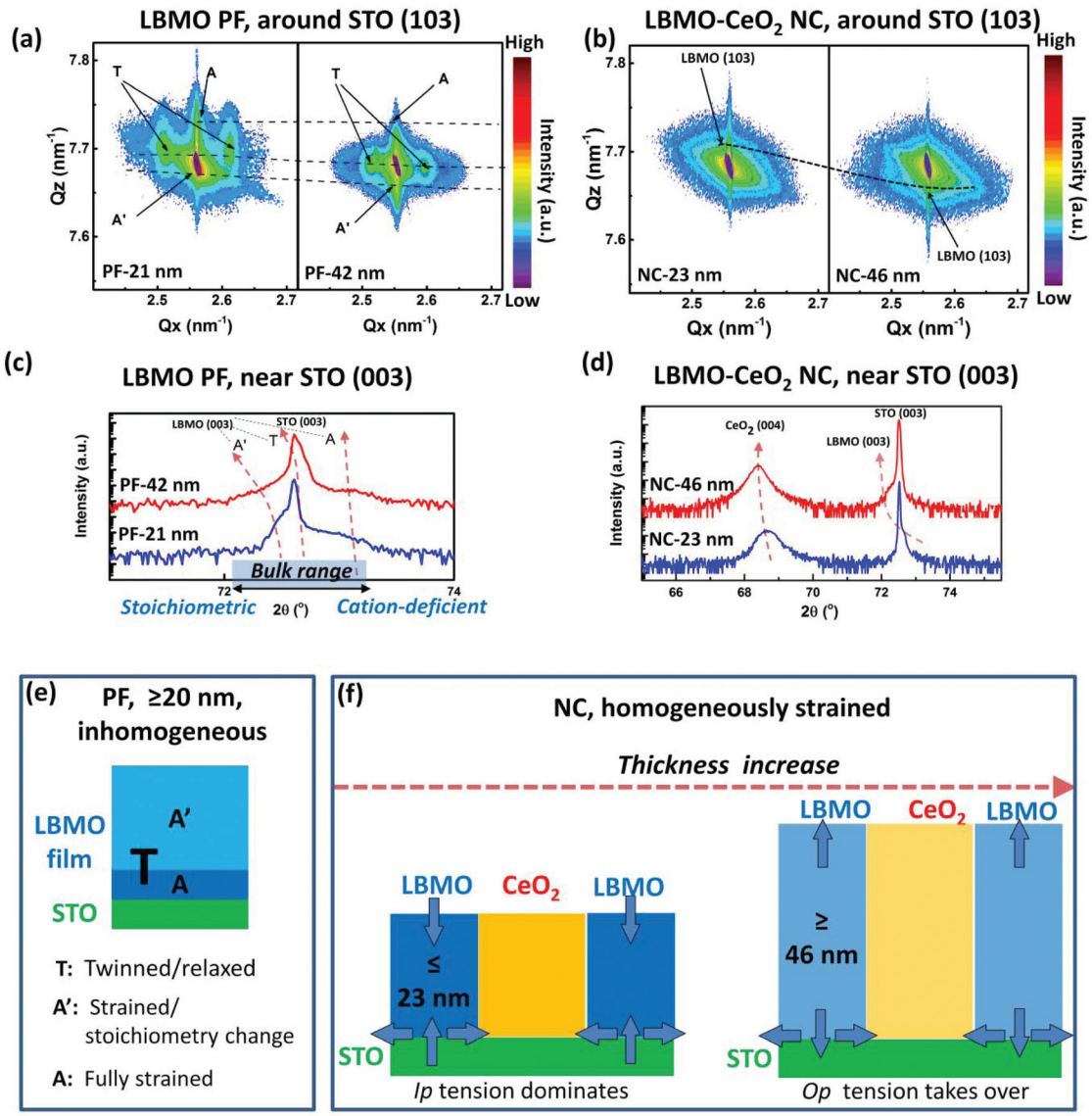

Fig. 3 Asymmetric reciprocal space maps (RSM) around the STO (103) peak for (a) the LBMO plain films (PF) with increasing thickness and (b) the LBMO–CeO_2 nanocomposite (NC) films with increasing thickness. Symmetric XRD ω–2θ scans near the STO (003) peak for (c) the LBMO PF and (d) the LBMO–CeO_2 NC films. The blue shadowed area shows the range for the peak positions of reported bulk lattice constants of $La_{0.9}Ba_{0.1}MnO_3$. (e) Illustration of the phase coexistence in the PF. A lighter color corresponds to a larger lattice constant. The illustrated thickness regions are not to scale. (f) Illustration of strain tuning in the LBMO–CeO_2 NC films when thickness is increasing. A lighter color corresponds to a larger lattice constant.

TEM structural analysis on the 100 nm PF is also provided in ESI S7.† A boundary of strain variation is found at around 17 nm, as shown in the geometric phase analysis (GPA) strain mapping in Fig. S7b,† which indicates the relaxation from phase A to A′. Besides, diffraction spot splitting is observed in the SAED patterns in the film part (as shown in Fig. S7a†), which additionally proves the existence of the twinning phase.

Phase A has ip tension to match the STO substrate lattice parameter (3.905 Å), with a corresponding op compression. Hence, the (003) peak for A is at a higher angle than STO (003) in the 2θ–ω scan. This phase is likely cation deficient since its lattice parameter should be <3.905 Å, in order to achieve ip tension. Non-stoichiometry in thin manganites is a well-known mechanism for strain accommodation.[39] Hence, apart from oxidation-atmosphere-induced cation vacancies as in bulk samples, strain is an additional driving force for the cation vacancy formation observed here.

For phase A′, the (003) peaks of LBMO are at a lower angle than STO (003), which would suggest op tension of the A′ phase, at least if it were strained to the STO. This would mean it had larger lattice parameters than STO, indicating it to be more stoichiometric than A. It is likely that A′ is stable towards the upper part of the film and is more stoichiometric because it doesn't need to change its stoichiometry so much to accommodate the substrate strain. The op lattice parameter of A′ expands rapidly with thickness, and reaches 3.923 Å when the thickness of the PF reaches 100 nm (Fig. S6†).

It is noted that a wide lattice parameter (psudocubic) range for $La_{0.9}Ba_{0.1}MnO_3$ bulk and films has been reported in the literature, from ~3.88–3.92 Å,[11,13,51,66–68] and this range is shown in Fig. 3c and Fig. S5a.† The range is consistent with variations in cation non-stoichiometry, with a smaller lattice parameter indicating a greater cation deficiency. The calculated lattice constants of the PFs range from 3.883 Å (A phase) in the 21 nm PF (Fig. 3) to 3.923 Å (A′ phase) in the 100 nm PF (Fig. S5a†). This is consistent with the range of lattice parameters reported for bulk LBMO, confirming again the susceptibility of LBMO (whether bulk or films) to non-stoichiometry and structural modulation.

The T phase is characterized by a pair of twinning peaks (T), which indicates the presence of periodically tilted unit cells, as indicated in Fig. 3a and Fig. S5a.† Periodic octahedral tilting of the MnO_6 octahedra occurs in manganites as an energy efficient way to accommodate lattice mismatch strain[69,70] rather than conventional tetragonal deformation or stoichiometry change. The T phase is not constrained by the STO lattice ip, as determined by the Q_x peaks for T being at a different position to the STO peak in the reciprocal space maps of Fig. 3a. Hence, the T phase is towards the upper region of the film,[71] as we predict A′ to be also.

The fact that the rapidly changing lattice constant of the A′ phase has little influence on the T_c indicates that the T phase has the most dominant effect on the magnetic and transport properties of the PFs. The presence of the T phase in all PF films in the upper region explains the almost constant T_M (T_c) with film thickness in the PFs (recall Fig. 1a and c). Extensive studies have shown that twinning is one mechanism for partial or total relaxation to the bulk lattice structure[69] and the twinning starts to appear above a certain thickness.[71] Therefore, for the PFs studied here, for the same or very similar levels of relaxation in the T phase, no matter if it is a partial or total relaxation, the T_M (or T_c) will stay almost constant.

Now we turn to discussing the phases and strain states of the NC films. From the RSMs and 2θ–ω scans (Fig. 3b and d), we observe only one homogeneous LBMO phase with a sharp (103) or (003) X-ray peak, which somewhat overlaps with the STO (103) or (003) peak. This contrasts to the inhomogeneous phases observed in the PF.

All the films are ip strained by STO as observed by the same positions of the centres of the (103) peak Q_x values in Fig. 3b. In the thin NC films (23 nm), similar to the case of phase A in the PFs, vertical op compression results, as observed by the shoulder peak on the right hand side of the STO (003) peak, *i.e.* at higher 2θ in the 23 nm NC in Fig. 3d. The op compression is caused by the epitaxial ip tension induced by the STO substrate (a = 3.905 Å) on the smaller lattice parameter of $La_{0.9-x}Ce_xBa_{0.1}MnO_3$. Even though Ce filling of La vacancies tends to enlarge the LBMO lattice (c = 3.900 Å in the 23 nm NC, as compared to 3.883 Å of the A phase in the 21 nm PF), the lattice is still smaller than the vacancy-free $La_{0.9}Ba_{0.1}MnO_3$ bulk (a = 3.92 Å), because the Ce^{n+} (n = 3 or 4) has a smaller ionic radius than La^{3+}.[57,72] With increasing the thickness, *i.e.* for the 46 nm film, as observed by the shoulder peak shifting to the left hand side of the STO (003) peak in Fig. 3(d), the vertical strain state in LBMO is switched from op compression to op tension. Owing to the vertical clamping of the op lattice parameters by the CeO_2 nanocolumns, there is no elastic compensation of strain in the op direction as there is in the phase A of PFs.

A schematic diagram of the NC film strain state in Fig. 3f shows the strain tuning of the NC films. We note that for a >100 nm film thickness, the vertical tension stablizes and saturates (Fig. S5b†) while the ip strain remains the same since it is controlled by the substrate.

The op lattice parameters of the LBMO phase in the NC films are extracted by profile fitting of the 2θ–ω scans of Fig. 3d. The estimated op lattice parameter, c, changes from 3.900 Å (23 nm) to 3.910 Å (46 nm). For the 46 nm film, the op strain is increased by 0.25% compared to the 23 nm film where the substrate controls the film strain state. The slight strain increase is significant for reducing the DE coupling in lightly doped LBMO, as discussed later.

The strain state in the NC film is very different from the PF because in the PF a combination of different LBMO phases are formed for strain relaxation. In the NC film, on the other hand, vertical epitaxy between the sub-5 nm wide LBMO regions with the CeO_2 scaffold locks the strain vertically and laterally and, very importantly, makes it more uniform. We also note that the lateral width of the LBMO between the nanocolumns is below the reported minimum size (~20 u.c.) for the

formation of the twinning domains in manganites,[69] and this therefore precludes their formation.

We now analyse the connection between the strain and physical properties in the NC films. As discussed above, the T_cs of the PFs stay at around 212 K, which are higher than the bulk, owing mainly to non-stoichiometry effects, and we hypothesise that the T phase lies towards the film surface and dominates the measured T_c (T_M). Here it is not possible to determine the exact c for the T phase from the 2θ–ω scans, because the tilting of twin domains prevents accurate measurement of c. For the NC films the average LBMO op lattice constant tends to increase with thickness. At the same time, T_c decreases from 201 to 188 K, mirroring the rise in c, indicating that a stretch of the LBMO lattice reduces the DE coupling. Similarly, a sharp reversible dependence of T_c on c-axis was shown in previous work *via* He ion implantation in $La_{0.7}Sr_{0.3}MnO_3$ thin films.[73] Indeed, it is well established that epitaxial strain in manganites influences the Mn 3d e_g electron orbital occupancy or the Mn–O bond.[12,15,25,73] It is known that T_c in hole doped manganites is determined by DE interactions which are directly related to the transfer integral between neighbouring Mn ions through the oxygen bridge.[25]

In the NC films, c expands with increasing thickness while a axis remains unchanged, leading to an increase in the c/a ratio. A low c/a ratio (<1) is reported to enhance the electron occupancy of the ip $d_{x^2-y^2}$ orbital, which enhances the DE coupling and induces metallicity in lightly doped LBMO.[11] A high c/a ratio, on the other hand, is more favorable to the preferential occupancy of the $d_{3z^2-r^2}$ orbitals rather than the $d_{x^2-y^2}$ orbitals, leading to a reduction of the ip DE hopping integral t,[73] and to reduced DE. We recall that a 0.25% op strain increase was achieved in the 46 nm film compared to the 23 nm film. The corresponding c/a ratios are 0.999 and 1.001, which explains the much reduced DE coupling in the 46 nm film.

It is also worth noting that LBMO is fully ip strained by the STO and hence a tetragonal phase is maintained irrespective of thickness. If one assumes that the Mn–O bond angle θ of the tetragonal phase is unchanged,[74] for a constant θ with thickness, the DE hopping integral, t, as defined below[25]

$$t \propto d^{-3.5} \sin \theta/2 \quad (1)$$

will reduce with film thickness because the op bond length, d, increases. This is also consistent with the reduced DE coupling in the thicker films.

Previously, independent c and a straining has not been achieved in lightly doped lanthanum manganites. Also, uniform straining to induce a single-phase manganite has not been demonstrated. However, both these factors are critical for maintaining the FMI properties in thin films. It is clear from Fig. 3a and c that uniform straining in PFs is not possible merely *via* substrate strain engineering as strain relaxation and multiple phases are formed. As for bulk, mechanical and chemical pressure engineering of the structures have been undertaken but both these produce hydrostatic straining. Neither can be applied to thin films. Also, by those methods c and a cannot be independently tuned. On the other hand, the VAN method for straining enables precise tuning of the T_c of LBMO by expanding the c without reducing the a, resulting in an enhanced c/a ratio, and thus giving a novel way to carefully tune the DE coupling.

Conclusions

In summary, the problem that ferromagnetic insulating properties of lightly hole-doped manganite $La_{0.9}Ba_{0.1}MnO_3$ (LBMO) cannot be translated from bulk to films has been addressed in this study. We have shown a way to overcome this problem *via* Ce doping of films, giving rise to light Ce doping of LBMO and creation of a vertically aligned nanocomposite formed of stiff CeO_2 nanocolumns. The light Ce doping of the LBMO ensures filling of intrinsic cation vacancies, so as to reduce unwanted DE coupling and associated metallicity. The stiff nanopillars induce a ~0.25% uniform out-of-plane tension, and prevent strain relaxation of LBMO into different pseudo-cubic phases. This contrasts to plain LBMO (and other manganite) films which have the aforementioned problems and are non-insulating. This is the first time that deliberate doping from VAN nanopillars has been used. It is also, as far as known, the first demonstration of the ability to achieve a single structural phase in manganites, where normally several pseudo-cubic structures form upon strain relaxation. The work represents a new way to nanoengineering ferromagnetic insulating properties into manganite films.

Experimental section

Sample preparation

$La_{0.9}Ba_{0.1}MnO_3$-CeO_2 (molar ratio 1 : 1) nanocomposite films were grown on single crystalline $SrTiO_3$ (001) substrates *via* a one-step process using pulsed laser deposition (PLD). A composite PLD target was prepared using a conventional solid-state sintering: stoichiometric and high-purity La_2O_3, Mn_2O_3 and BaO powders were mixed, grounded and sintered at 900 °C for 40 h and then re-ground and pelletized after mixing with CeO_2, followed by an additional sintering at 1100 °C for 9 h. During deposition, the oxygen partial pressure and the growth temperature were maintained at 0.2 mbar and 720 °C, respectively. A KrF excimer laser with a 248 nm wavelength was used. The repetition rate and laser fluency were 1 Hz and 1 J cm^{-2}, respectively. After deposition, the sample was cooled down to room temperature under an oxygen pressure of 0.4 atm with a cooling rate of 10 °C min^{-1}.

Sample characterization

The structure of the films was characterized with a Panalytical Empyrean high resolution X-ray diffraction (XRD) system. Cross-sectional and plain view images of the film were obtained by high resolution transmission electron microscopy (HRTEM) FEI TALOS F200X at 200 kV equipped with ultrahigh

resolution high angle annular dark field detectors and Super-X™ electron-dispersive X-ray spectroscopy. The samples for the TEM analysis were obtained through mechanical grinding, dimpling, and a final ion milling step. Magnetic and transport property measurements were performed using a Superconducting Quantum Interference Device (SQUID) magnetometer (MPMS, Quantum Design) and a Physical Properties Measurement System (PPMS, Quantum Design). Platinum electrodes were deposited by DC sputtering for standard four-probe characterization of the transport properties. X-ray photoemission spectroscopy was used to study the valence band of the films by a monochromatic Al $K_{\alpha 1}$ X-ray source ($h\nu$ = 1486.6 eV) using a SPECS PHOIBOS 150 electron energy analyzer with a total energy resolution of 500 meV. To prevent charging effects during the measurements, the samples were grown on (001) Nb-STO substrates, while all the other samples were grown on undoped STO substrates.

Author contributions

J.L.M.-D. and C.Y. conceived the ideas. J.L.M.-D., E.-M.C. and W.L. supervised the research. C.Y. and S.C. made the samples, C.Y. carried out XRD characterization. C.Y. and W.L. performed electrical properties measurement. C.Y., R.W. conducted the magnetic properties characterization. W. L. carried out XPS measurement. X.S, J.J., S.X. and H.Y.W. performed TEM imaging. C.Y., J.L.M.-D., W.L., E.-M.C. and T.M. contributed to data analysis. C.Y. and J.L.M.-D. wrote the manuscript. All authors contributed to reviewing the data in this manuscript and commenting on the manuscript.

Conflicts of interest

The authors declare no conflict of interests.

Acknowledgements

The authors acknowledge Dr Mary Vickers, Dr John Walmsley, Dr Jingwei Hou, Tiesheng Wang and Yisong Lin for discussion and support. The Cambridge investigators acknowledge funding from the Leverhulme Trust grant RPG-2015-017, EPSRC grants EP/N004272/1 and EP/M000524/1, and the Isaac Newton Trust in Cambridge (minute 16.24(p)). T. M. and J. L. M.-D. acknowledge funding from EU grant H2020-MSCA-IF-2016 745886 MuStMAM. C. Y. thanks the Cambridge Commonwealth, European & International Trust for funding. X. S., J. J., S. X. and H. W. acknowledge the U.S. National Science Foundation (DMR-1565822) for the microscopy work at Purdue University.

Notes and references

1 W. S. Choi, K. T. Kang, H. Jeen, Z. Gai and H. N. Lee, *Curr. Appl. Phys.*, 2017, **17**, 722–726.
2 R. Ramesh and N. A. Spaldin, *Nat. Mater.*, 2007, **6**, 21–29.
3 S. Baidya and T. Saha-Dasgupta, *Phys. Rev. B: Condens. Matter Mater. Phys.*, 2011, **84**, 035131.
4 M. A. Subramanian, A. P. Ramirez and W. J. Marshall, *Phys. Rev. Lett.*, 1999, **82**, 1558–1561.
5 B. T. Matthias, R. M. Bozorth and J. H. Van Vleck, *Phys. Rev. Lett.*, 1961, **7**, 160–161.
6 J. E. Kleibeuker, E.-M. Choi, E. D. Jones, T.-M. Yu, B. Sala, B. A. MacLaren, D. Kepaptsoglou, D. Hernandez-Maldonado, Q. M. Ramasse, L. Jones, J. Barthel, I. MacLaren and J. L. MacManus-Driscoll, *NPG Asia Mater.*, 2017, **9**, e406.
7 B. Vertruyen, R. Cloots, J. S. Abell, T. J. Jackson, R. C. da Silva, E. Popova and N. Keller, *Phys. Rev. B: Condens. Matter Mater. Phys.*, 2008, **78**, 094429.
8 U. Lüders, M. Bibes, K. Bouzehouane, E. Jacquet, J.-P. Contour, S. Fusil, J.-F. Bobo, J. Fontcuberta, A. Barthélémy and A. Fert, *Appl. Phys. Lett.*, 2006, **88**, 082505.
9 Y. Tokura and Y. Tomioka, *J. Magn. Magn. Mater.*, 1999, **200**, 1–23.
10 A.-M. Haghiri-Gosnet and J.-P. Renard, *J. Phys. D: Appl. Phys.*, 2003, **36**, R127–R150.
11 J. Zhang, H. Tanaka, T. Kanki, J.-H. Choi and T. Kawai, *Phys. Rev. B: Condens. Matter Mater. Phys.*, 2001, **64**, 184404.
12 T. Kanki, H. Tanaka and T. Kawai, *Phys. Rev. B: Condens. Matter Mater. Phys.*, 2001, **64**, 224418.
13 P. Murugavel, J. H. Lee, J. G. Yoon, T. W. Noh, J. S. Chung, M. Heu and S. Yoon, *Appl. Phys. Lett.*, 2003, **82**, 1908–1910.
14 L. Yin, C. Wang, Q. Shen and L. Zhang, *RSC Adv.*, 2016, **6**, 96093–96102.
15 A. Suwardi, B. Prasad, S. Lee, E. Choi, P. Lu, W. Zhang, L. Li, M. Blamire, Q. Jia, H. Wang, K. Yao and J. L. MacManus-Driscoll, *Nanoscale*, 2016, **8**, 8083–8090.
16 C. Zhou and D. M. Newns, *J. Eng. Appl. Sci.*, 1997, **82**, 3081–3088.
17 T. L. Meyer, L. Jiang, S. Park, T. Egami and H. N. Lee, *APL Mater.*, 2015, **3**, 126102.
18 Y. Tokura, *Rep. Prog. Phys.*, 2006, **69**, 797–851.
19 Y. Moritomo, H. Kuwahara and Y. Tokura, *Physica B: Condens. Matter*, 1997, **237–238**, 26–27.
20 P. G. Radaelli, G. Iannone, M. Marezio, H. Y. Hwang, S. W. Cheong, J. D. Jorgensen and D. N. Argyriou, *Phys. Rev. B: Condens. Matter Mater. Phys.*, 1997, **56**, 8265–8276.
21 X. G. Chen, J. B. Fu, C. Yun, H. Zhao, Y. B. Yang, H. L. Du, J. Z. Han, C. S. Wang, S. Q. Liu, Y. Zhang, Y. C. Yang and J. B. Yang, *J. Appl. Phys.*, 2014, **116**, 103907.
22 R. Mbatang, D. Xue, E. Enriquez, R. Yuan, H. Han, P. Dowden, Q. Wang, E. Fohtung, D. Xue, T. Lookman, S. J. Pennycook and A. Chen, *Nanoscale*, 2019, **11**, 7364–7370.
23 W. Li, J. E. Kleibeuker, R. Wu, K. H. L. Zhang, C. Yun and J. L. MacManus-Driscoll, *Phys. Rev. B: Condens. Matter Mater. Phys.*, 2017, **96**, 165103.

24 P. Murugavel, J. H. Lee, K.-B. Lee, J. H. Park, J.-S. Chung, J.-G. Yoon and T. W. Noh, *J. Phys. D: Appl. Phys.*, 2002, **35**, 3166–3170.
25 Q. Yuan, *Phys. Rev. B: Condens. Matter Mater. Phys.*, 2004, **70**, 066401.
26 M. Huijben, L. W. Martin, Y.-H. Chu, M. B. Holcomb, P. Yu, G. Rijnders, D. H. A. Blank and R. Ramesh, *Phys. Rev. B: Condens. Matter Mater. Phys.*, 2008, **78**, 094413.
27 P. D. C. King, H. I. Wei, Y. F. Nie, M. Uchida, C. Adamo, S. Zhu, X. He, I. Božović, D. G. Schlom and K. M. Shen, *Nat. Nanotechnol.*, 2014, **9**, 443–447.
28 V. Moshnyaga, in *Frontiers in Magnetic Materials*, Springer-Verlag Berlin Heidelberg GmbH, Berlin, 2005, pp. 415–458.
29 H. L. Ju, Y. S. Nam, J. E. Lee and H. S. Shin, *J. Magn. Magn. Mater.*, 2000, **219**, 1–8.
30 J. L. Macmanus-Driscoll, *Adv. Funct. Mater.*, 2010, **20**, 2035–2045.
31 A. Chen, Z. Bi, Q. Jia, J. L. MacManus-Driscoll and H. Wang, *Acta Mater.*, 2013, **61**, 2783–2792.
32 J. L. MacManus-Driscoll, P. Zerrer, H. Wang, H. Yang, J. Yoon, A. Fouchet, R. Yu, M. G. Blamire and Q. Jia, *Nat. Mater.*, 2008, **7**, 314–320.
33 J. L. MacManus-Driscoll, A. Suwardi, A. Kursumovic, Z. Bi, C. F. Tsai, H. Wang, Q. Jia and O. J. Lee, *APL Mater.*, 2015, **3**, 062507.
34 S. A. Harrington, J. Zhai, S. Denev, V. Gopalan, H. Wang, Z. Bi, S. A. T. Redfern, S. H. Baek, C. W. Bark, C. B. Eom, Q. Jia, M. E. Vickers and J. L. MacManus-Driscoll, *Nat. Nanotechnol.*, 2011, **6**, 491–495.
35 V. Moshnyaga, B. Damaschke, O. Shapoval, A. Belenchuk, J. Faupel, O. I. Lebedev, J. Verbeeck, G. van Tendeloo, M. Mücksch, V. Tsurkan, R. Tidecks and K. Samwer, *Nat. Mater.*, 2003, **2**, 247–252.
36 A. Chen, J.-M. Hu, P. Lu, T. Yang, W. Zhang, L. Li, T. Ahmed, E. Enriquez, M. Weigand, Q. Su, H. Wang, J.-X. Zhu, J. L. MacManus-Driscoll, L.-Q. Chen, D. Yarotski and Q. Jia, *Sci. Adv.*, 2016, **2**, e1600245.
37 F. Sandiumenge, J. Santiso, L. Balcells, Z. Konstantinovic, J. Roqueta, A. Pomar, J. P. Espinós and B. Martínez, *Phys. Rev. Lett.*, 2013, **110**, 107206.
38 J. L. MacManus-Driscoll, A. Suwardi and H. Wang, *MRS Bull.*, 2015, **40**, 933–942.
39 J.-L. Maurice, F. Pailloux, A. Barthélémy, O. Durand, D. Imhoff, R. Lyonnet, A. Rocher and J.-P. Contour, *Philos. Mag.*, 2003, **83**, 3201–3224.
40 H.-S. Lee, T. Mizoguchi, T. Yamamoto, S.-J. L. Kang and Y. Ikuhara, *Acta Mater.*, 2007, **55**, 6535–6540.
41 A. Vailionis, H. Boschker, W. Siemons, E. P. Houwman, D. H. A. Blank, G. Rijnders and G. Koster, *Phys. Rev. B: Condens. Matter Mater. Phys.*, 2011, **83**, 064101.
42 S. C. Wimbush, M. Li, M. E. Vickers, B. Maiorov, D. M. Feldmann, Q. Jia and J. L. MacManus-Driscoll, *Adv. Funct. Mater.*, 2009, **19**, 835–841.
43 L. Gerward, J. Staun Olsen, L. Petit, G. Vaitheeswaran, V. Kanchana and A. Svane, *J. Alloys Compd.*, 2005, **400**, 56–61.
44 V. Kanchana, G. Vaitheeswaran, A. Svane and A. Delin, *J. Phys.: Condens. Matter*, 2006, **18**, 9615–9624.
45 C. Zhu, R. Zheng, J. Su and J. He, *Appl. Phys. Lett.*, 1999, **74**, 3504–3506.
46 S. Sankarrajan, K. Sakthipandi, P. Manivasakan, K. Thyagarajan and V. Rajendran, *Phase Transitions*, 2011, **84**, 657–672.
47 R. V. K. Mangalam and A. Sundaresan, *J. Chem. Sci.*, 2006, **118**, 99–103.
48 J. Mizusaki, N. Mori, H. Takai, Y. Yonemura, H. Minamiue, H. Tagawa, M. Dokiya, H. Inaba, K. Naraya, T. Sasamoto and T. Hashimoto, *Solid State Ionics*, 2000, **129**, 163–177.
49 C. Zener, *Phys. Rev.*, 1951, **82**, 403–405.
50 L. Hu, Z. Sheng, X. Hu, R. Zhang, B. Wang, W. Song and Y. Sun, *J. Phys. D: Appl. Phys.*, 2012, **45**, 175002–175006.
51 B. Dabrowski, K. Rogacki, X. Xiong, P. W. Klamut, R. Dybzinski and J. Shaffer, *Phys. Rev. B: Condens. Matter Mater. Phys.*, 1998, **58**, 2716–2723.
52 W. Pan, P. Lu, J. F. Ihlefeld, S. R. Lee, E. S. Choi, Y. Jiang and Q. X. Jia, *Phys. Rev. Mater.*, 2018, **2**, 021401(R).
53 M. Fan, W. Zhang, F. Khatkhatay, L. Li and H. Wang, *J. Appl. Phys.*, 2015, **118**, 065302.
54 A. Chen, Z. Bi, H. Hazariwala, X. Zhang, Q. Su, L. Chen, Q. Jia, J. L. MacManus-Driscoll and H. Wang, *Nanotechnology*, 2011, **22**, 315712.
55 L. Shen, C. Ma, S. Cheng, S. Ren, S. Cheng, S. Mi and M. Liu, *J. Mater. Chem. C*, 2016, **4**, 10955–10961.
56 X. Sun, J. Huang, J. Jian, M. Fan, H. Wang, Q. Li, J. L. MacManus-Driscoll, P. Lu, X. Zhang and H. Wang, *Mater. Horiz.*, 2018, **5**, 536–544.
57 W. Zhu, J. Jin, X. Chen, C. Li, T. Wang, C. Tsang and C. Liang, *Environ. Sci. Pollut. Res.*, 2018, **25**, 5643–5654.
58 B. C. Morris, W. R. Flavell, W. C. Mackrodtb and M. A. Morris, *J. Mater. Chem.*, 1993, **3**, 1007–1013.
59 W. Lee, S.-Y. Chen, E. Tseng, A. Gloter and C.-L. Chen, *J. Phys. Chem. C*, 2016, **120**, 14874–14882.
60 H. Shi, T. Hussain, R. Ahuja, T. W. Kang and W. Luo, *Sci. Rep.*, 2016, **6**, 31345.
61 H. Chou, C. B. Wu, S. G. Hsu and C. Y. Wu, *Phys. Rev. B: Condens. Matter Mater. Phys.*, 2006, **74**, 174405.
62 N. N. Loshkareva, K. N. Mikhalev, I. A. Fogel, A. V. Mostovshikova, E. V. Korolev, N. I. Solin, Y. P. Sukhorukov, S. V. Naumov, A. M. Kostromitina, N. V. Balbashov and N. V. Lukin, *Fiz. Metody Issled. Met.*, 2003, **95**, 23–30.
63 D. K. Mishra, D. R. Sahu, P. K. Mishra, S. K. Singh, B. K. Mohapatra and B. K. Roul, *Bull. Mater. Sci.*, 2011, **34**, 1501–1506.
64 T. Shibata, B. Bunker, J. F. Mitchell and P. Schiffer, *Phys. Rev. Lett.*, 2002, **88**, 207205.
65 F. A. Kröger and H. J. Vink, *J. Phys. Chem. Solids*, 1958, **5**, 208–223.

66 V. A. Cherepanov, E. A. Filonova, V. I. Voronin and I. F. Berger, *J. Solid State Chem.*, 2000, **153**, 205–211.
67 B. M. Nagabhushana, G. T. Chandrappa, R. P. S. Chakradhar, K. P. Ramesh and C. Shivakumara, *Solid State Commun.*, 2005, **136**, 427–432.
68 P. Mandal and B. Ghosh, *Phys. Rev. B: Condens. Matter Mater. Phys.*, 2003, **68**, 014422.
69 U. Gebhardt, N. V. Kasper, A. Vigliante, P. Wochner, H. Dosch, F. S. Razavi and H. U. Habermeier, *Phys. Rev. Lett.*, 2007, **98**, 096101.
70 A. Vigliante, U. Gebhardt, A. Rühm, P. Wochner, F. S. Razavi and H. U. Habermeier, *Europhys. Lett.*, 2001, **54**, 619–625.
71 J. Santiso, L. Balcells, Z. Konstantinovic, J. Roqueta, P. Ferrer, A. Pomar, B. Martínez and F. Sandiumenge, *CrystEngComm*, 2013, **15**, 3908.
72 C. He, H. Ji, Z. Huang, T. Wang, X. Zhang, Y. Liu, M. Fang, X. Wu, J. Zhang and X. Min, *J. Phys. Chem. C*, 2018, **122**, 15659–15665.
73 H. Guo, S. Dong, P. Rack, J. Budai, C. Beekman, Z. Gai, W. Siemons, C. Gonzalez, R. Timilsina, A. T. Wong, A. Herklotz, P. C. Snijders, E. Dagotto and T. Z. Ward, *Phys. Rev. Lett.*, 2015, **114**, 256801.
74 E. M. Choi, A. Kursumovic, O. J. Lee, J. E. Kleibeuker, A. Chen, W. Zhang, H. Wang and J. L. Macmanus-Driscoll, *ACS Appl. Mater. Interfaces*, 2014, **6**, 14836–14843.